Electron-phonon interaction in perovskite nanocrystals in fluorophosphate glass matrix

© *M.N. Bataev*[1], *M.S. Kuznetsova*[1], *D.V. Pankin*[1], *M.B. Smirnov*[1], *S.Yu. Verbin*[1], *I.V. Ignatiev*[1], *I.A. Eliseyev*[2], *V.Yu. Davydov*[2], *A.N. Smirnov*[2], *E.V. Kolobkova*[3,4]

[1] St. Petersburg State University,
198504 St. Petersburg, Russia
[2] Ioffe Institute of RAS,
194021 St. Petersburg, Russia
[3] ITMO University,
199034 St. Petersburg, Russia
[4] St. Petersburg State Institute of Technology (Technical University),
190013 St. Petersburg, Russia

E-mail: batae1996@gmail.com

The photoluminescence (PL) spectra of $CsPbBr_3$ perovskite nanocrystals grown in a fluorophosphate glass matrix exhibit phonon replicas of the exciton line. The dependence of intensity of the phonon replica on its number is simulated taking into account the difference in the curvature of the excited and ground adiabatic potentials. The Raman spectra of $CsPbBr_3$ nanocrystals are measured. Calculations based on the density functional theory is performed to obtain the spectrum of phonon states of these crystals in the orthorhombic phase. The phonon frequencies observed in the PL and Raman spectra are compared with the calculation results.

Keywords: perovskites, nanocrystals, Raman scattering, phonon replicas, $CsPbBr_3$, fluorophosphate glass.

1. Introduction

Perovskite nanocrystals (NCs) are actively studied today due to their wide potential for practical applications [1–4]. The energy of optical transitions depends on the chemical composition and the size of nanocrystals. This makes it possible to easily vary the transition energy over the entire visible spectral range. Recently synthesized perovskite NCs encapsulated in glass matrices [5–8] represent a new class of optical materials. Perovskite nanocrystals $CsPbX_3$ (X = Cl, Br, I) synthesized in a fluorophosphate glass matrix [8] exhibit several advantages over colloidal analogues. In particular, they possess high stability of physical and optical properties

The demonstration of high quantum yield of photoluminescence (PL) in perovskite NCs has stimulated numerous studies of the energy structure and crystalline phases of perovskites, see for example recent papers [4,9–11] and references therein. It has been established that impurity levels are practically absent in the bandgap [9,12], which provides a high quantum yield of PL. At the same time, metastable exciton states with a lifetime of the order of tens of microseconds are present in perovskite NCs [13]. The presence of these states leads to an interesting effect of anti-Stokes PL [14–17]. Moreover, these states exhibit long-lived spin dynamics, which holds promise for the realization of quantum technologies [13,18–21].

The studies of phonon states and exciton-phonon interaction in perovskite NCs play an important role in the understanding of the NC properties [22–25]. Experimental investigations of the phonon spectrum at various temperatures of the nanocrystals, combined with theoretical modelings, provide valuable information about the structural phase transitions.

One of the methods for studying phonons is the Raman scattering spectroscopy (the RS spectroscopy). It can provide the data to determine the crystal structure and the nature of interatomic interactions in the objects being studied. To get a clearer idea of phonon states, the Raman spectroscopy data should be supplemented by analysis of infrared absorption spectra (IR spectra). This is especially important for crystals with a centrosymmetric structure, which include the compounds investigated in this study. These are polar optical phonons that play a decisive role in the mechanism of exciton-phonon interaction [26]. Polar optical phonons are inactive in the Raman scattering. Calculations based on the density functional theory (DFT) make it possible to clarify the information obtained from spectroscopic studies. It helps to interpret phonon spectra.

In this study, phonon spectrum of the orthorhombic modification of the $CsPbBr_3$ crystal is investigated theoretically and experimentally. A comparison of the calculated and experimental Raman spectra made it possible to confirm the structural model of the nanocrystals under study. Observed spectral peaks were correlated with certain phonon states. The calculated IR-absorption spectrum allowed to propose an interpretation of the phonon-related features observed in the PL spectra.

2. Sample fabrication process and characterization of samples

The sample under study is a fluorophosphate (FP) glass with the composition of $60Ba(PO_3)_2-15NaPO_3-12AlF_3-1Ga_2O_3-4Cs_2O-8PbF_2$ (mol%), doped with 3.4 mol% of $BaBr_2$, which was produced by melt quenching. The choice of a FP glass matrix for the formation of $CsPbBr_3$ NCs is motivated by the possibility of injecting high concentrations of halides. The glass was synthesized in a closed glassy carbon crucible at $T = 1000-1050\,°C$. About 50 g of mixed powder was melted in the crucible for 20 min. As a result, nearly colorless glass was produced. To form nanocrystals, the glass was kept for 240 min at a glass transition temperature $T = 400\,°C$.

The fact of NCs formation and identification of their sizes were implemented using X-ray patterns recorded by a Rigaku X-ray diffractometer. Several weak diffraction peaks were observed, indicating the formation of $CsPbBr_3$ crystalline phases. The NC size was determined by the Scherrer formula: $d = K\lambda/(\beta \cos\theta)$, where d is the mean size of ordered (crystalline) domains, which can be less or equal to the size of NC. Parameter K is a dimensionless form-factor. Its typical value is of about 0.9 but varies depending on the actual shape of the crystallite. Parameter β is the line full width at the half maximum of intensity in radians taking into account the instrumental line broadening. Quantity θ is the Bragg angle in radians, $\lambda = 0.154$ nm is the X-ray wavelength. In our case the parameters were as follows: $2\theta = 30.4°$, $\theta = 15.2°$, $\beta = 0.64°$ ($\beta = 0.011$ rad). Based on the analysis of X-ray patterns, the diameter of NCs in the sample under study turned out to be 13 nm.

3. Experimental technique and calculation procedure

The non-resonant PL and the spectrum of phonon replicas in resonant PL was studied using the standard technique of stationary spectroscopy. Sample were placed in a helium closed-cycle cryostat and cooled down to temperature of 11 K. The measurements were carried out in the reflection geometry. A laser with the radiation photon energy of $E_{exc} = 3.06$ eV was used as a light source to study the non-resonant PL. The laser radiation was directed to the sample at a small angle to the optical axis. As a result, reflected laser beam did not enter the lens aperture in the PL collection channel. An iHR-550 spectrometer was used (the focal length of 550 mm, the diffraction grating with 1200 gr/mm) to record the PL spectrum. The spectrometer is equipped with a low noise nitrogen cooled CCD camera Symphony II. Measurement of the resonant PL were carried out using a laser with the radiation photon energy of $E_{exc} = 2.33$ eV. This optical excitation corresponds to the low-energy edge of the PL band of the $CsPbBr_3$ NCs ensemble.

The PL excitation spectra were measured using the same setup. An incandescent lamp with a MDR-4 monochromator were used as an adjustable monochromatic radiation source. The PL excitation spectra were normalized to the intensity of the portion of the lamp spectrum selected by the monochromator. The use of CCD-camera allowed the excitation spectra to be recorded simultaneously over the entire PL band of the sample under study.

Measurements of the Raman scattering (RS) spectra were performed using a T64000 spectrometer equipped with a confocal microscope. Sample were cooled down to the temperature of $T = 7$ K. A laser with a radiation photon energy of $E_{exc} = 1.96$ eV was used as an optical excitation source. The measurements were carried out in the backscattering geometry. The RS of studied samples with $CsPbBr_3$ nanocrystals grown in FP glass is characterized by low ratio signal/noise. Therefore, the RS spectra of the FP glass matrix without nanocrystals, as well as the spectrum of the air were, additionally measured and subtracted from the RS signal of the glass with NCs.

The electronic structure and phonon spectra were calculated using the generalized gradient approximation (GGA) of the density functional theory with the PBE functional and norm-conserving pseudopotential in the Castep program (Material Studio) [27,28]. The cutoff energy value when compiling the plane-wave basis was 1200 eV. To solve the electronic problem, a field self-consistency criterion was set equal to $5 \cdot 10^{-7}$ eV/atom. The k-grid dimension was chosen to be $3 \times 2 \times 3$ (with a step of $0.04\,\text{Å}^{-1}$). The geometry was optimized until residual forces and stresses reached values not exceeding 0.01 eV/Å and 0.02 GPa, respectively. For the optimized structure, phonon frequencies were calculated by the linear response method (DFPT) [29].

4. Photoluminescence under resonant excitation

Figure 1 shows the resonant PL spectrum of a sample with $CsPbBr_3$ NCs measured under resonant excitation to the low-energy edge of the PL band by laser radiation with a photon energy of $E_{exc} = 2.33$ eV ($\lambda_{exc} = 532$ nm). Red arrow indicates the energy of laser radiation. The insert to Figure 1 shows PL spectrum of the same sample under short-wave excitation with a photon energy of $E_{exc} = 3.06$ eV ($\lambda_{exc} = 405$ nm). In Figure 1, three phonon replicas 18 meV apart from each other can be clearly seen on the background of the PL tail. Phonon replicas corresponds to the vibration frequency of $\nu = 150$ cm^{-1}.

The PL excitation spectra measured at different PL detection energies ($E_{det} = 2.375$, 2.380, 2.385 eV) shown on Figure 2. Detection energies corresponds to the high-energy edge of the PL band (see the inset in Figure 1). As it can be seen in the Figure 2, several broad peaks are observed in the studied spectral region.

The leftmost peak shifts to the left side of the spectrum as the energy of the detected photons E_{det} increases. This

feature of the spectrum is presumably associated with the resonant excitation of excitons into the second quantum-confined state of excitons in the studied NCs. As E_{det} increases, the size of the NCs decreases in the subensemble from which the PL is recorded. Accordingly, the energy
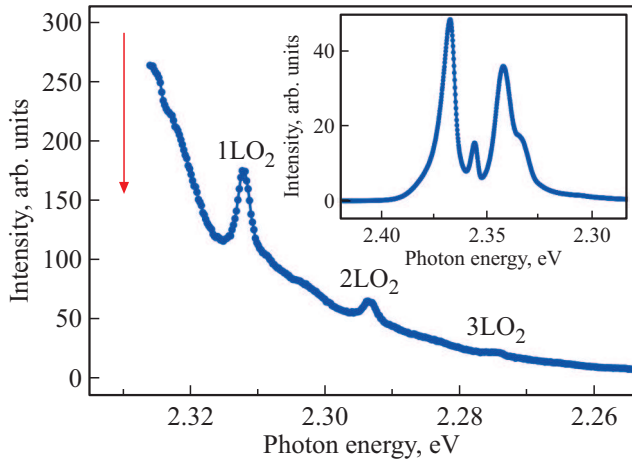
Figure 1. The resonant PL spectrum under excitation of CsPbBr$_3$ NCs by laser radiation with a photon energy of $E_{exc} = 2.33$ eV ($\lambda_{exc} = 532$ nm). The red arrow indicates the energy of photons of the optical excitation. A number of LO phonon replicas corresponding to frequencies that are multiples of $150\,cm^{-1}$ ($18\,meV$) can be seen on the background of the PL tail. The inset in the figure shows the PL spectrum measured under excitation by laser radiation with a photon energy of $E_{exc} = 3.06$ eV ($\lambda_{exc} = 405$ nm). The measurements were taken at the temperature of $T = 11$ K.
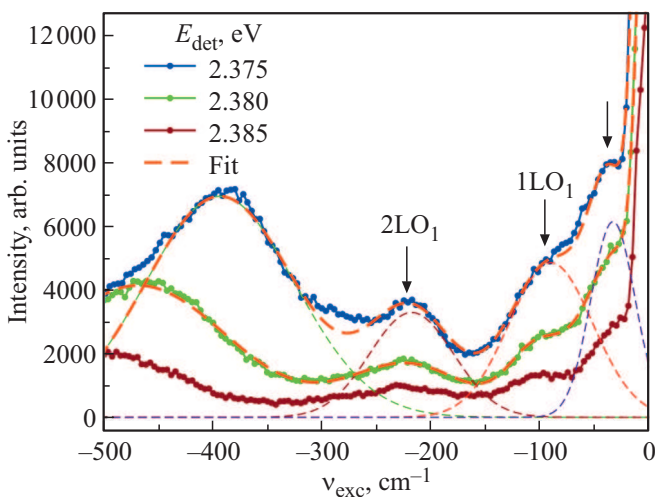
Figure 2. PL excitation spectra measured at different PL detection energies given in the legend. The horizontal axis shows the difference between the detection energies of PL and the excitation photons in reciprocal centimeters. The intense signal observed in the region $< 25\,cm^{-1}$ is associated with the scattered radiation from the light source. The dashed curves show the decomposition of the spectrum into Gaussian contours and the fitting of these spectra by the sum of these contours. $T = 11$ K. (The colored version of the figure is available on-line).
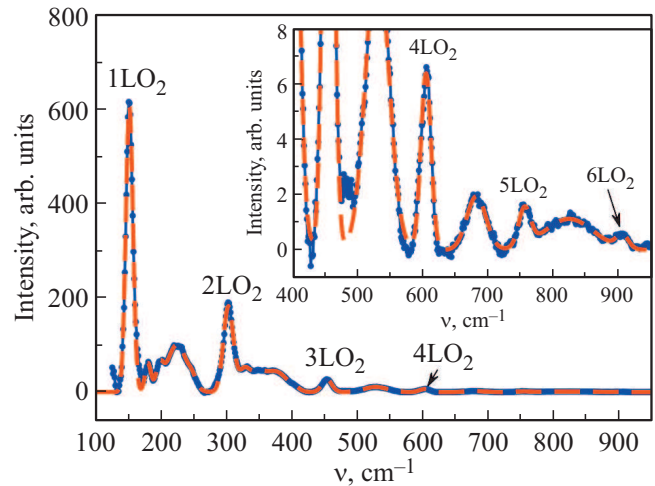
Figure 3. Spectrum of phonon replicas of CsPbBr$_3$ NCs under resonant excitation of PL, $E_{exc} = 2.33$ eV ($\lambda_{exc} = 532$ nm). The smooth PL component is subtracted. Dashed line shows the fitting by sum of Gaussian contours. The inset shows 100 times zoomed part of the spectrum in the region of $400-950\,cm^{-1}$. $T = 11$ K.

of the first and subsequent quantum-confined exciton levels increases, as well as does the energy gap between them. This increment of the energy gap leads to the shift of the observed peak in the PL excitation spectrum.

Other features of the PL excitation spectrum observed in Figure 2 (shown with arrows) at frequencies of $\nu_{exc} \approx -217, -107, -39\,cm^{-1}$ retain their positions nearly unchanged relative to E_{det}. Therefore, we assume that these features in the PL excitation spectra are due to exciton-phonon transitions. In other words, these transitions are caused by simultaneous creation of exciton and phonons with the above-specified frequencies. In this case, the frequency of $107\,cm^{-1}$ corresponds to the creation of one LO-phonon, and the frequency of $217\,cm^{-1}$ corresponds to the creation of two LO-phonons. It should be noted that the LO phonon frequency in the excited state of the electronic system ($\nu_1 \approx 108\,cm^{-1}$) is significantly lower than LO phonon frequency in the ground state ($\nu_2 = 150\,cm^{-1}$). Such inequality of the phonon frequencies indicates significant difference in the curvature of the adiabatic potentials in the ground and excited electronic states.

5. Spectrum of phonon states

Resonant PL has been measured with long signal accumulation time for detail study of the phonon spectrum. Figure 3 shows the measured spectrum with dynamic range of 3 decimal orders. Smooth component of the PL signal was subtracted from the spectrum. Due to the accumulation of the signal, we were able to detect the 6 highest-frequency phonon replicas with frequency of $\nu_2 = 150\,cm^{-1}$. The theoretical calculation described below allows us to identify this phonon state. It related
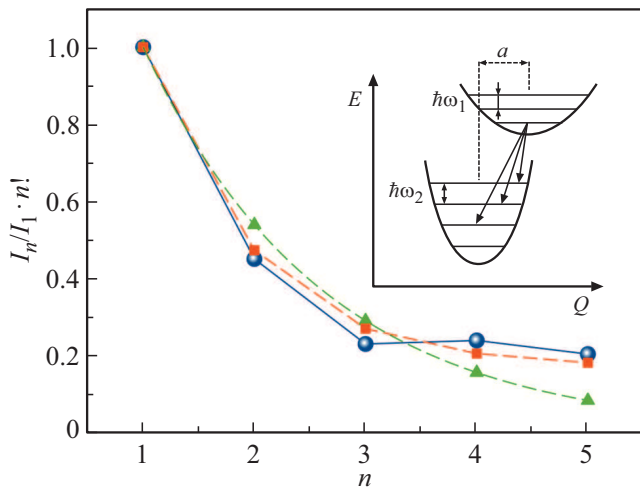
Figure 4. $I_n/I_1 \cdot n!$ value as a function of phonon replica number. Blue dots show experimentally obtained values, green triangles show approximation in the Huang–Rhys model ($S = 0.54$), red squares show the calculation within the model [35]. The inset shows the diagram of adiabatic potentials and observed optical transitions. Parameter a describes the shift of the minima of the adiabatic potentials.

to a longitudinal optical (LO) vibration corresponding to antiphase displacements of cations and anions.

Blue dots in Figure 4 show the dependence of the intensity of exciton-phonon transitions normalized to the intensity of the first peak and multiplied by $n!$, where n is the number of the phonon replica. This allows us to show the intensities of all peaks within the same decimal order. The inset to Figure 4 schematically shows the Franck–Condon model [30–32]. Within this model the behavior of phonon replicas is analyzed. This model uses an adiabatic approximation to separate the electronic and vibrational degrees of freedom and a parabolic approximation for adiabatic potentials. The potential minima are shifted relative to each other by a certain value of a. The curvature of the potentials is also different, which describes the difference in vibration frequencies measured in the resonant PL and PL excitation spectra. The exciton-phonon transitions observed in the experiment are shown in the diagram by arrows.

The one-dimensional Schrödinger equation for a harmonic oscillator is solved to theoretically model the intensity of phonon replicas [33]

$$-\frac{\hbar^2}{2m} \frac{\partial^2}{\partial x^2} \psi_n(x) + \frac{m\omega^2 x^2}{2} \psi_n(x) = E_n \psi_n(x). \quad (1)$$

Let us reduce this equation from standard notation to a dimensionless form by replacing the variable:

$$Q = \sqrt{\frac{m\omega}{\hbar}} x. \quad (2)$$

Then the Schrödinger equation takes the following form:

$$\frac{\partial^2}{\partial Q^2} \psi_n(Q) + \left(\frac{2E_n}{\hbar\omega} - Q^2\right) \psi_n(Q) = 0. \quad (3)$$

The wave functions of vibrational states are obtained as a result of solving the Schrödinger equation:

$$\psi_n(Q) = \left(\frac{1}{\pi}\right)^{1/4} \frac{1}{\sqrt{2^n n!}} \exp\left(-\frac{Q^2}{2}\right) H_n(Q), \quad (4)$$

where $H_n(Q)$ are Hermite polynomials.

The curvature parameter of adiabatic potentials is determined by the following ratio:

$$\beta_{1,2} = \frac{m\omega_{1,2}^2}{2}, \quad (5)$$

where $\omega_{1,2} = 2\pi\nu_{1,2}$. Let us introduce the ratio of curvature of adiabatic potentials, $\beta = \beta_1/\beta_2 = \omega_1^2/\omega_2^2$. We will assume that wave function (4) describes vibrational states in the lowest electronic state. The wave function of the upper state is obtained by replacing the variable, $Q_1 = \sqrt[4]{\beta}(Q - a)$. This expression takes into account the shift of the upper adiabatic potential and the change in its curvature. Taking also into account the change in normalization, the vibrational wave function in the upper state has the following form:

$$\psi_n'(Q) = \sqrt[4]{\frac{\sqrt{\beta}}{\pi}} \frac{1}{\sqrt{2^n n!}} \exp\left(-\frac{Q_1^2}{2}\right) H_n(Q_1). \quad (6)$$

Optical transition between lowest vibrational level in the upper electronic state and different vibrational levels in the ground electronic state are observed in the resonant PL spectrum. According to the Frank–Condon model, intensities of these transitions are determined by the square of the modulus of the overlap integral of vibrational wave functions:

$$I_n = \left| \int_{-\infty}^{-\infty} \psi_0'(Q)\psi_n(Q)dQ \right|^2. \quad (7)$$

Let us first consider the simplest case, the Huang–Rhys model [34]. It is assumed that the curvature of the lower and upper adiabatic potentials is the same ($\beta = 1$) and, accordingly, $\omega_1 = \omega_2$. In this model, the integrals of overlap are easily calculated analytically. Expression for the intensity of transitions takes the following simple form:

$$I_n = e^{-S} \frac{S^n}{n!}, \quad (8)$$

where $S = a^2/2$. Figure 4 shows the fitting of the experiment by the $I_n/I_1 \cdot n! = S^{n-1}$ dependence, which follows from the above expression. The optimal value of the model parameter determined by the least square method is $S = 0.54$ ($a = 1.04$). It can be seen that this model provides very rough approximation of the intensity behavior of phonon replicas. This should be expected,

because $\omega_1 \neq \omega_2$ as it follows from the resonant PL and PL excitation spectra.

For a more strict description of the intensities of phonon replicas, we have calculated the overlap integrals included in expression (7), taking into account different curvatures of adiabatic potentials $(\beta = \beta_1/\beta_2 \neq 1)$. In this case, analytical formulae can also be obtained for expression (7). They are given in [35] for the first few vibrational states. Figure 4 shows the dependence obtained within this model for the optimal values of its parameters: $a = 0.7$ and $\sqrt{\beta} = \omega_1/\omega_2 = 0.8$. It can be seen that this model provides a more accurate description of the experiment. However, the resulted frequency ratio is slightly different from the ratio obtained from the spectra of PL excitation and resonant PL $(\sqrt{\beta} = \omega_1/\omega_2 = 0.7)$. The discrepancy is probably due to the error in determining the ω_1 frequency and the ratio of phonon replicas intensities, as well as due to the approximation nature of the model [35].

6. Theoretical modeling of phonon spectra

Structure with the minimum energy of the electronic subsystem has been found at the first stage of the theoretical study. Such a structure was found as a result of complete (both with respect to the cell parameters and with respect to atomic positions) optimization of the geometry of the orthorhombic modification of $CsPbBr_3$ with space group *Pnma* and four formula units in the cell. Theoretical estimates of the cell parameters (8.402, 11.756, and 8.179 Å) turned out to be close to those found experimentally (8.186, 11.659, and 8.098 Å) [36].

Then the zone-center phonon states were calculated. All modes were divided into irreducible representations of the symmetry group. For all inversion-invariant modes (so-called g-modes), their intensities in the RS spectra were determined. According to the group theory, for the orthorhombic modification, 24 active RS modes are predicted for the Γ-point: $7A_g + 5B_{1g} + 7B_{2g} + 5B_{3g}$. The calculated depolarized RS-spectrum of the orthorhombic phase of $CsPbBr_3$ is shown in Figure 5. The full width at half maximum of the peak is taken equal to $2\,cm^{-1}$.

It can be seen that two intense lines at frequencies of 67 and $74\,cm^{-1}$ are dominating in the calculated spectrum. The corresponding phonons with A_g and B_{2g} symmetry are bending vibrations of $PbBr_6$ octahedra. In the experimental RS spectrum, which is also shown in Figure 5, these peaks can be associated with a double peak with maxima at 70 and $76\,cm^{-1}$.

The high-frequency line near $115\,cm^{-1}$ is associated with A_g and B_{3g} symmetry modes corresponding to asymmetric stretching vibrations localized in Pb−Br−Pb bridges. In the experimental RS spectrum, these peaks can be associated with a peak with a broad maximum at about $125\,cm^{-1}$. Three less intense peaks with frequencies of 30, 44 and $58\,cm^{-1}$ are associated with scattering by phonons of A_g
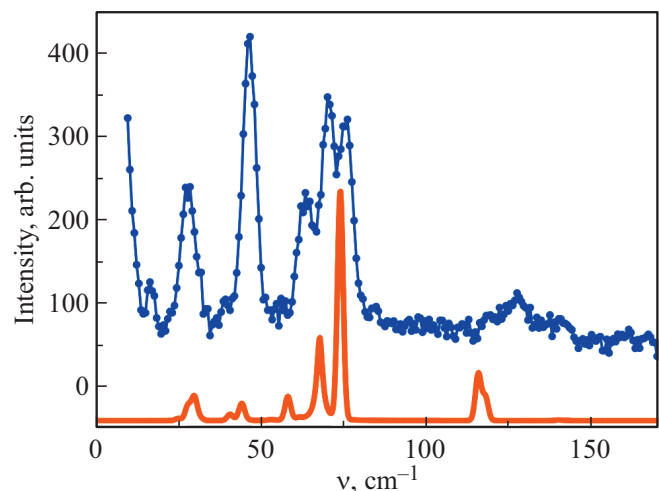
Figure 5. RS spectrum of $CsPbBr_3$ NC (blue line), measured at a temperature of $7\,K$, and the calculated spectrum of phonons for the orthorhombic phase (red line).

symmetry. Corresponding peaks can be found in the experimental RS spectrum as well.

It should be noted that there are discrepancies between the predicted peak intensities in the calculated RS spectrum and those obtained experimentally. Possible reasons for these differences are the quantum confined effect and the influence of the glass matrix.

Modes, which are anti-invariant to inversion (so-called u-modes), are inactive in the RS spectrum but active in IR spectra. According to the group theory, for the Γ-point in the IR spectra, 28 active modes are predicted: $10B_{1u} + 10B_{2u} + 8B_{3u}$. For all transverse optical (TO) modes, we have calculated the oscillator forces and determined the spectrum of the corresponding longitudinal optical (LO) modes. The intensities in the IR absorption spectra were calculated for all TO and LO modes.

It has been shown in a number of studies [37,38], that electron-phonon and exciton-phonon interactions in a $CsPbBr_3$ crystal are mainly determined by the scattering of carriers by LO phonons (the so-called Fröehlich mechanism). Therefore, special attention has been paid to the spectrum of LO modes to interpret the resonant PL spectrum. For phonons of the B_{1u}, B_{2u}, and B_{3u} representations polarized in different crystallographic directions, frequencies and shapes of LO modes were calculated and their IR intensities were determined. We used this IR spectrum to model phonon replicas in the PL spectra.

According to our calculations, in each direction there is only one, the most high-frequency LO-mode in the set that has noticeable IR intensity. Therefore, a conclusion can be made that the main 1LO−6LO phonon replicas shown in Figure 3 are most likely formed exactly by these modes. The calculated frequency of this vibration is $\nu \approx 140\,cm^{-1}$, which is well consistent with the experimental frequency of $\nu_2 = 150\,cm^{-1}$. However, broad additional features in
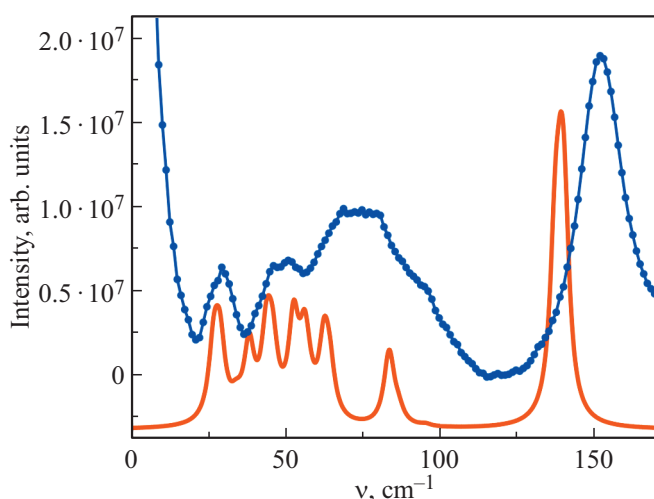
Figure 6. Phonon replicas spectrum between 1LO and 2LO peaks. The red curve shows the calculated IR absorption spectrum summed over different directions of the wave vector **k**.

the experimentally measured PL spectrum are observed between the main phonon replicas. Presumably, their presence is associated with the manifestation of other, less active LO phonons. Figure 6 shows the part of the PL spectrum between the first and the second phonon replicas. The position of the first phonon replica is taken as the starting point. In the single-crystal case, the spectrum of phonon replicas depends on the polarization of the excitation and the orientation of the crystal relative to the radiation. Accordingly, LO phonons with a certain polarization should be used to interpret such a spectrum. Due to the fact that the object of our study is an ensemble of disordered nanocrystals grown in glass, the spectrum of phonon replicas neither depends on polarization nor on orientation of the sample. In this case, the spectrum of LO phonons should be averaged over the polarization direction. Such a spectrum, calculated for the orthorhombic phase $CsPbBr_3$, is shown with the red curve in Figure 6. The full width at half maximum of phonon peaks is taken equal to $2\,cm^{-1}$.

It can be seen that, in general, the pattern of the spectrum plotted according to calculation results corelates with the frequency distribution of features observed in the experimental PL spectrum.

7. Conclusion

Phonon replicas in the resonant photoluminescence spectrum of $CsPbBr_3$ nanocrystals were discovered and experimentally studied. Dependence of integral intensity of the phonon replicas on their number has been theoretically modeled. The modelling allowed us to estimate the ratio of the curvature parameters for adiabatic potentials of the excited and ground electronic states in the $CsPbBr_3$ NCs. The modeling results are further confirmed by experimental

measurements of phonon frequencies in the excited and ground electronic states of the system. Microscopic modeling of phonon states in the NCs has been performed. According to the modeling, only one phonon mode in the spectrum of polar phonons should be most intense in the PL spectra, which is confirmed experimentally. A comparison of the experimental Raman scattering spectra and calculations suggests that $CsPbBr_3$ NCs grown in a fluorophosphate glass matrix has an orthorhombic crystal lattice. Discrepancies in the experimental and theoretical phonon spectra may be due to the effect of quantum confinement and the influence of the glass matrix.

Conflict of interest

The authors declare that they have no conflict of interest.

References

[1] L. Protesescu, S. Yakunin, M.I. Bodnarchuk, F. Krieg, R Caputo, C.H. Hendon, R.X. Yang, A. Walsh, M.V. Kovalenko. Nano Lett., **15** (6), 3692 (2015).
[2] P. Ramasamy, D.-H. Lim, B. Kim, S.-H. Lee, M.-S. Lee, J.-S. Lee. Chem. Commun., **52**, 2067 (2016).
[3] X. Li, Y. Wu, S. Zhang, B. Cai, Y. Gu, J. Song, H. Zeng. Advanced Functional Mater., **26** (15), 2435 (2016).
[4] M.A. Becker, R. Vaxenburg, G. Nedelcu, P.C. Sercel, A. Shabaev, M.J. Mehl, J.G. Michopoulos, S.G. Lambrakos, N. Bernstein, J.L. Lyons, T. Stoferle, R.F. Mahrt, M.V. Kovalenko, D.J. Norris, G. Raino, A.L. Efros. Nature, **553**, 189 (2018).
[5] P. Li, C. Hu, L. Zhou, J. Jiang, Y. Cheng, M. He, X. Liang, W. Xiang. Mater. Lett., **209** (C), 483 (2017).
[6] S. Liu, Y. Luo, M. He, X. Liang, W. Xiang. J. Eur. Ceramic Soc., **38** (4), 1998 (2018).
[7] Y. Ye, W. Zhang, Z. Zhao, J. Wang, C. Liu, Z. Deng, X. Zhao, J. Han. Adv. Opt. Mater., **7** (9), 1801663 (2019).
[8] E. Kolobkova, M. Kuznetsova, N. Nikonorov. J. Non-Cryst. Sol., **563**, 120811 (2021).
[9] A.O. Murzin, N.I. Selivanov, V.O. Kozlov, I.I. Ryzhov, T. Miyasaka, A.V. Emeline, Y.V. Kapitonov. Adv. Opt. Mater., **9** (18), 2001327 (2021).
[10] T. Yamada, T. Handa, Y. Yamada, Y. Kanemitsu. J. Phys. D: Appl. Phys., **54** (38), 383001 (2021).
[11] S. Liu, A.R. DeFilippo, M. Balasubramania n, Z. Liu, S.G. Wang, Y.-S. Chen, S. Chariton, V. Prakapenka, X. Luo, L. Zhao, J.S. Martin, Y. Lin, Y. Yan, S.K. Ghose, T.A. Tyson. Adv. Sci., **8** (18), 2003046 (2021).
[12] R. Brakkee, R.M. Williams. Appl. Sci., **10** (9), 3061 (2020).

[13] V.V. Belykh, M.L. Skorikov, E.V. Kulebyakina, E.V. Kolob-kova, M.S. Kuznetsova, M.M. Glazov, D.R. Yakovlev. Nano Lett., **22** (11), 4583 (2022).

[14] X. Ma, F. Pan, H. Li, P. Shen, C. Ma, L. Zhang, H. Niu, Y. Zhu, S. Xu, H. Ye. J. Phys. Chem. Lett., **10** (20), 5989 (2019).

[15] A. Granados del'Aguila, T.T.H. Do, J. Xing, J.J. Wen, J.B. Khurgin, Q. Xiong. Nano Res., **13**, 1962 (2020).

[16] W. Zhang, Y. Ye, C. Liu, J. Wang, J. Ruan, X. Zhao, J. Han. Adv. Opt. Mater., **9** (6), 2001885 (2021).

[17] M.N. Kuznetsova, Maria S. and Bataev, M.A. Chukeev, N.D. Rostovtsev, S.Y. Verbin, I.V. Ignatiev, V.Y. Davydov, A.N. Smirnov, I.A. Eliseev, E.V. Kolobkova. Opt. Spectrosc., **130** (11), 1472 (2022).

[18] S. Strohmair, A. Dey, Y. Tong, L. Polavarapu, B.J. Bohn, J.Feld-mann. Nano Lett., **20** (7), 4724 (2020).

[19] M.J. Crane, L.M. Jacoby, T.A. Cohen, Y. Huang, C.K. Luscombe, D.R. Gamelin. Nano Lett., **20** (12), 8626 (2020).

[20] P.S. Grigoryev, V.V. Belykh, D.R. Yakovlev, E. Lhuillier, M. Bayer. Nano Lett., **21** (19), 8481 (2021).

[21] E. Kirstein, N.E. Kopteva, D.R. Yakovlev, E.A. Zhukov, E.V. Kolobkova, M.S. Kuznetsova, V.V. Belykh, I.A. Yugova, M.M. Glazov, M. Bayer, A. Greilich. Nature Commun., **14** (699) (2023).

[22] R. Saran, A. Heuer-Jungemann, A.G. Kanaras, R.J. Curry. Adv. Opt. Mater., **5** (17), 1700231 (2017).

[23] Y. Guo, O. Yaffe, T.D. Hull, J.S. Owen, D.R. Reichman, L.E. Brus. Nature Commun., **10** (1), 1175 (2019).

[24] Y. Yamada, Y. Kanemitsu. NPG Asia Mater., **14** (1), 48 (2022).

[25] K. Cho, H. Tahara, T. Yamada, H. Suzuura, T. Tadano, R. Sato, M. Saruyama, H. Hirori, T. Teranishi, Y. Kanemitsu. Nano Lett., **22** (18), 7674 (2022).

[26] C.M. Iaru, A. Brodu, N.J.J. van Hoof, S.E.T. ter Huurne, J. Buhot, F. Montanarella, S. Buhbut, P.C.M. Christianen, D. Vanmaekelbergh, C. de Mello Donega, J.G. Rivas, P.M. Koenraad, A.Yu. Silov. Nature Commun., **12** (1), 5844 (2021).

[27] S.J. Clark, M.D. Segall, C.J. Pickard, P.J. Hasnip, M.I.J. Probert, K. Refson, M.C. Payne. Zeitschriftf'ur Kristallogr. — Crystalline Mater., **220** (5−6), 567 (2005).

[28] K. Refson, P.R. Tulip, S.J. Clark. Phys. Rev. B, **73**, 155114 (2006).

[29] X. Gonze, C. Lee. Phys. Rev. B, **55**, 10355 (1997).

[30] J. Franck, E.G. Dymond. Trans. Faraday Soc., **21**, 536 (1926).

[31] E. Condon. Phys. Rev., **28**, 1182 (1926).

[32] P. Atkins. *Molecular quantum mechanics* (Oxford Univ. Press, Oxford, 2005).

[33] L.D. Landau, L.M. Lifshitz. *Quantum Mechanics Non-Relativistic Theory*. 3rd edn (Pergamon Press Ltd, 1965) v. 3, 67.

[34] K. Huang, A. Rhys, N.F. Mott. Proc. Royal Society of London. Ser. A. Math. Phys. Sci., **204** (1078), 406 (1950).

[35] V.S. Krivobok, S.N. Nikolaev, V.S. Bagaev, S.I. Chentsov, E.E. Onishchenko, A.A. Pruchkina. JETP Lett., **114** (2), 98 (2021).

[36] M. Szafrański, A. Katrusiak, K. Stähl. J. Mater. Chem. A, **9**, 10769 (2021).

[37] C.M. Iaru, J.J. Geuchies, P.M. Koenraad, D. Vanmaekelbergh, A.Y. Silov. ACS Nano, **11** (11), 11024 (2017).

[38] X. Zhou, Z. Zhang. AIP Advances, **10** (12), 125015 (2020).

Translated by Y.Alekseev